

The relative contributions of scattering and viscoelasticity to the attenuation of S waves in Earth's mantle

Susini deSilva¹, Vernon F. Cormier¹

¹Department of Physics, University of Connecticut, 196 Auditorium Road, Storrs, CT 06269, USA

Correspondence to: Vernon F. Cormier (vernon.cormier@uconn.edu)

Abstract. The relative contributions of scattering and viscoelastic attenuation to the apparent attenuation of seismic body waves are estimated from synthetic and observed S waves multiply reflected from Earth's surface and the core-mantle boundary. The synthetic seismograms include the effects of viscoelasticity and scattering from small-scale heterogeneity predicted from both global tomography and from thermodynamic models of mantle heterogeneity that have been verified from amplitude coherence measurements of body waves observed at dense arrays. Assuming thermodynamic models provide an estimate of the maximum plausible power of heterogeneity measured by elastic velocity and density fluctuations, we predict a maximum scattering contribution of 43 % to the total measured attenuation of mantle S waves having a dominant frequency of 0.05 Hz. The contributions of scattering in the upper and lower mantle to the total apparent attenuation are estimated to be roughly equal. The relative strength of the coda surrounding observed ScSn waves from deep focus earthquakes is not consistent with a mantle having zero intrinsic attenuation.

1 Introduction

Seismic tomography reveals a laterally heterogeneous velocity structure in the mantle. Constraining the locations and dimensions of such elastic heterogeneities is critical to understanding the intricate details of the dynamic mixing process of the mantle, which is closely tied to the plate tectonic evolution of the Earth. Large-scale (~ 1000 km) heterogeneities are likely caused by the buoyancy differences that drive thermal-chemical convection. The effects of thermal diffusion, however, limit small-scale (~ 1 to 100 km) heterogeneities to chemical variations. Small-scale heterogeneities can scatter 0.1 to 1 Hz. body waves, transferring energy from body wave pulses observed at a receiver to later time windows and receivers (Shearer, 2015). Mantle attenuation measured from P and S waves will hence always be a summation of a scattering and an intrinsic viscoelastic attenuation. The viscoelastic dispersion of dominantly intrinsic attenuation successfully explains the lower velocities of Earth models derived from low frequency free oscillations observed in the millihertz band from those derived from 1 Hz body waves (Dziewonski and Anderson, 1981). Yet some extrapolations of the scale lengths and intensities of heterogeneity inferred from high frequency body waves have suggested attenuation in the mantle may instead be dominated by scattering (Ricard et al., 2014, Sato, 2019).

34 The apparent attenuation of multiple ScS waves is an excellent observable to untangle the relative contributions of
35 scattering and intrinsic attenuation. Many previous studies have used ScS and its reverberations within the mantle to
36 obtain path averaged values for the mantle attenuation. These attenuation measurements are usually represented in
37 terms of a quality factor (Q or Q_{ScS} for ScS-based measurements). The estimates of these apparent attenuation
38 measurements include both the intrinsic or viscoelastic attenuation of the wave amplitude and the attenuation caused
39 by scattering effects. In this work we will consider the apparent attenuation ($\frac{1}{Q_{ScS}}$) to be the addition of intrinsic
40 attenuation ($\frac{1}{Q_{intr}}$) and scattering attenuation ($\frac{1}{Q_{scat}}$) for path averaged observations of SH waves reflected from the
41 free surface and core-mantle boundary. The intrinsic component accounts for the loss of energy due to friction and
42 heat loss as the wave propagates through the mantle with different viscous properties caused by the motion of
43 defects in the crystalline lattice structure of silicates or by the motion of melt at grain boundaries or in pores.
44 Intrinsic attenuation manifests itself in body waves by amplitude decay, pulse broadening, and velocity dispersion.
45 The scattering attenuation accounts for the energy loss that is scattered into different directions as elastic
46 heterogeneities are encountered along the path of a body wave. In addition to amplitude decay and pulse broadening
47 of the main phase, scattering generates increased levels of coda energy comprised of redistributed energy arriving
48 later than the main phase. Many past studies calculating the apparent attenuation of multiple ScS use spectral
49 amplitude ratios (Kovach and Anderson, 1964, Yoshida and Tsujiura, 1975, Sipkin and Jordan, 1980, Lay and
50 Wallace, 1983) and time domain amplitude ratios (Kanamori and Riviera, 2015) of adjacent ScS waveforms. An
51 alternative analysis technique seeks the attenuation operator that converts an ScS_{n-1} waveform into an ScS_n
52 waveform (Jordan and Sipkin, 1977, Revenaugh and Jordan, 1989). Sipkin and Revenaugh (1994) concluded that a
53 frequency domain approach works better for Q_{ScS} measurements, especially in continental regions that tend to have
54 lower shear Q values compared to oceanic regions. Lee et al. (2003) compared observations and numerical
55 simulations of coda envelope offsets before and after ScS synthesized with two-layer scattering models
56 superimposed on a PREM reference model to calculate the scattering contribution to total attenuation measurements.
57 They concluded that scattering loss dominates intrinsic loss in the lower mantle.

58

59 Our effort employs an estimate for a ScS_n attenuation operator to evaluate the relative percentages of scattering and
60 intrinsic attenuation contributing to the apparent attenuation observed from simulated mantle heterogeneity models.
61 Observations of scattered body waves together with geodynamic modeling have established that heterogeneities of
62 scale lengths as small as 4 to 10 km with RMS (root mean square) velocity perturbations of 1 to 8 % can persist
63 throughout the mantle, even in the presence of constant convective stirring (Hedlin et al., 1997, Shearer and Earl,
64 2008, Kaneshima and Helffrich, 2010). Our investigation considers the effects of similar dimensions and
65 perturbation strengths for heterogeneity models. We also consider the effects of a model of mantle heterogeneity
66 power obtained by applying stochastic tomography (Zheng and Wu, 2009) to invert for the heterogeneity spectrum
67 of the upper 1000 km of the mantle from observations of amplitude and phase fluctuations of teleseismic P waves
68 observed by the Earthscope USArray (Cormier, et al.). We assumed fluctuations of S velocity and density to be
69 correlated with those of P velocity such that $\Delta V_S/V_S = 2 \Delta V_P/V_P$ and $\Delta \rho/\rho = 0.8 \Delta V_P/V_P$, taking the resultant depth-

70 dependent power spectrum to be a maximum plausible model of mantle heterogeneity. With these assumptions, the
71 power of the heterogeneity spectrum of S velocity closely matches those predicted by thermodynamically
72 constrained estimates of mantle chemistry and phase. Such models (e.g., Stixrude and Lithgow-Bertelloni, 2007)
73 predict significantly higher heterogeneity than the models of global tomography. Although the assumed chemistry
74 and potential temperature of thermodynamic models have been shown to affect average mantle velocities, the depth
75 position of predicted heterogeneity peaks and their maximum power, concentrated around mantle phase transitions,
76 are relatively unaffected (Stixrude and Lithgow-Bertelloni, 2012).

77

78 **2 Method**

79

80 **2.1 Models**

81

82 Apparent attenuations are measured from ScSn waveforms observed in synthetic seismograms for 4 different models
83 of mantle heterogeneity. All of these assume PREM as the one dimensional background velocity and density model,
84 with the PREM shear wave attenuations providing the purely intrinsic component of attenuation. Model 1 does not
85 perturb PREM with any lateral heterogeneities. Therefore, the apparent attenuation measured for this case will be
86 purely intrinsic. Model 2 (Fig.1) applies a depth-dependent shear velocity perturbation to the PREM mantle similar
87 to those determined from many seismic tomographic studies (Megnin and Romanowicz, 2000, Ritsema et al., 2004).
88 Model 3 (Fig. 2) applies scaled shear velocity and density perturbations to the PREM mantle based on the stochastic
89 P tomography model of Cormier et al. (2019) for the upper 1000 km of the mantle. Model 4 (Fig. 3) is the same as
90 Model 3 in the upper 1000 km of the mantle but includes an additional peak in heterogeneity power in the
91 lowermost mantle predicted by Stixrude and Lithgow-Bertelloni (2012) from the effect of the post-perovskite phase
92 transition. In Model 5, the intrinsic attenuations are turned off while still applying the thermodynamic model of
93 mantle heterogeneity to shear velocity perturbations. Hence the synthetic seismograms for this model will exhibit
94 purely scattering effects in any attenuation measurement. In all models, heterogeneities are represented as stochastic
95 random media with an exponential autocorrelation having a corner scale equal to 10 km. In Models 2, 3, 4, and 5 we
96 assume a relation between P velocity and density and shear velocity perturbations such that $\Delta\rho/\rho = 0.8 \Delta V_p/V_p$
97 and $\Delta V_s/V_s = 2 \Delta V_p/V_p$. The value for density perturbation in a mantle close to neutral buoyancy is relatively large,
98 but is commonly assumed in studies of crustal and upper mantle scattering based on Birch's law (Birch, 1952).

99

100 **2.2 Apparent attenuation measurements**

101

102 All simulations are performed by a numerical pseudospectral method in 2-D (Cormier, 2000), assuming an SH line
103 source at 500 km depth with a Gaussian-shaped source-time function having a half-width of 1.2 seconds. Wave
104 propagation uses a 2D staggered grid of radial step size 3.0 km and lateral step size 5.427 km, with time sampling
105 set to 0.025 seconds ensuring stability and negligible grid dispersion. Intrinsic attenuation, taken to be
106 approximately constant across a broad frequency band, is introduced by three memory functions using the methods

107 described by Robertson et al., (1994). Waveforms are computed at a great circle distance of 18° in order to avoid
 108 contamination of ScSn phases with depth phases or other nearby arrivals. These are corrected for 3D geometric
 109 spreading, and a line-to-point source conversion is made. Although 2D and 2.5D simulations neglect the effects of
 110 out-of-plane scattering, a comparison of 2-5D with 3D scattering simulations by Wu and Irving (2017) suggests that
 111 the neglect of out-of-plane scattering on the coda of teleseismic body waves are small. For each of the 5 models a 2-
 112 parameter attenuation operator (Eq. 1) is determined that converts the ScS waveform into an ScSScS waveform.
 113 Each attenuation operator depends on Q_{ScS} and the high frequency corner ($1/\tau_m$) of a relaxation spectrum, where
 114 attenuation is constant for 5 decades of frequency.

115 In the inversion procedure, the predicted ScSScS velocity waveform is generated by convolving the ScS waveform
 116 with an attenuation operator corresponding to a peak attenuation $1/Q_{ScS}$ and a high frequency corner $1/\tau_m$. A least
 117 squares norm is calculated (Eq. 2) for the difference between observed and predicted ScSScS velocity waveforms,
 118 which are aligned by the arrival times of first maximum and normalized by the peak-to-trough amplitudes (Fig. 4).
 119 A search over the two attenuation parameters is then performed to minimize an L2 norm difference to maximize a
 120 Gaussian probability density constructed using the L2 norm difference (Cormier et al., 1998). Half-widths of the
 121 probability density functions are used to infer errors.

122

123 An operator to convert an ScS waveform into an ScSScS waveform is defined in the frequency domain by

124

$$125 \quad O(\omega, Q, \tau) = \exp(-i\omega[\int_{ScSScS} \frac{ds}{\hat{v}(\omega)} - \int_{ScS} \frac{ds}{\hat{v}(\omega)}]) \quad (1)$$

126 where

$$\hat{V}(\omega, Q, \tau) = \frac{\sqrt{1 + \frac{2}{\pi Q_{ScS}^{-1} \ln\left(\frac{-i\omega + 1/\tau_l}{-i\omega + 1/\tau_m}\right)}}}{\sqrt{1 + \frac{2}{\pi Q_{ScS}^{-1} \ln\left(\frac{-i2\pi + 1/\tau_l}{-i2\pi + 1/\tau_m}\right)}}$$

127 and where

128 τ_l is the period of the low frequency corner in relaxation spectrum and $\frac{\tau_l}{\tau_m} = 10^5$

129 The least squares norm difference between observed and predicted waveforms is calculated from

130

$$131 \quad L2N(Obs, Pred) = \sqrt{\sum_t \frac{(Amp_{obs}(t) - Amp_{pred}(t))^2}{\sigma^2}} \quad (2)$$

132 where σ is a $\frac{noise}{signal}$ measurement from a 100 second time window preceding the ScSScS observation.

133

134 Our goal was to simply estimate an apparent attenuation parameter Q_{ScS} for the whole of the mantle when the effects
 135 of scattering are included rather than to seek a best fitting depth and frequency dependent attenuation model.

136 Accurate separation of depth from frequency dependence of attenuation benefits from observations of S and ScS
 137 over a range of source depths and distances as well as by an analysis of P waves to sample a broader frequency
 138 band. Nonetheless, our estimates for the high frequency corner parameter $1/\tau_m$ were bounded by estimates for $1/\tau_m$
 139 in the upper and lower mantle found by Choy and Cormier (1986).

140

141 3. Results

142

143 We found MODEL 1, which has pure intrinsic attenuation and no small-scale heterogeneity, to have an apparent
 144 attenuation value of 0.004167 corresponding to a $Q_{ScS} = 240$. This estimated Q_{ScS} value differs by only 2.2 % from
 145 the theoretical estimate of the depth averaged Q_{ScS} obtained for PREM with the relation $Q_{ScS} = (\int_{x_{ScSScS}} dt -$
 146 $\int_{x_{ScS}} dt) / (\int_{x_{ScSScS}} dt / Q_s(x) - \int_{x_{ScS}} dt / Q_s(x))$. Here x_{ScSScS} and x_{ScS} denote points along the path of
 147 ScSScS and ScS respectively, $Q_s(x)$ denote the Q_s values at those points read from 1D PREM. This result verifies
 148 the accuracy of the waveform L2 norm method for estimating Q_{ScS} .

149

150 With MODEL 2, which has a conventional tomographic estimate of mantle heterogeneity, we find that the apparent
 151 attenuation is increased to 0.005 (Q_{ScS} decreased to 200). Together with the knowledge of the purely intrinsic
 152 contribution ($\frac{1}{Q_{intr}}$) calculated in MODEL 1, the scattering component of attenuation ($\frac{1}{Q_{scat}}$) in MODEL 2 is
 153 estimated to be 0.000833. Hence the scattering caused by small-scale (~ 10 km) heterogeneities with a dVs/Vs depth
 154 profile similar to S20RTS (Ritsema et al., 2004), would account for 16.7 % of the measured ScS apparent
 155 attenuation. MODEL 3, which has a higher amount of heterogeneity due to increased Vs perturbations associated
 156 with predicted lateral variations in phase changes in the upper mantle, results in a higher apparent attenuation of
 157 0.005747 ($Q_{ScS} = 174$). MODEL 4, which includes additional heterogeneity predicted for the effects of a post-
 158 perovskite phase transition results in an even higher apparent attenuation of 0.007100 ($Q_{ScS} = 140$). We calculate
 159 that the scattering attenuation in the lower mantle (below 1000 km) and upper mantle (above 1000 km) of MODEL
 160 4 to be 0.0014 and 0.0016 with their percent contributions to the total apparent attenuation being 19.6 % and 22.4 %
 161 respectively. The overall scattering attenuation of MODEL 4 is 0.002933 with the scattering component accounting
 162 for 41.3 % of the measured ScS total apparent attenuation.

163 Finally, in MODEL 5 the intrinsic attenuation in the mantle is turned off while applying the mantle heterogeneity of
 164 MODEL 4. The apparent attenuation (now purely due to scattering) is measured to be 0.0029 ($Q_{ScS} = 340$). This high
 165 Q value lies towards the upper bound of regional estimates (~ 360) of Q_{ScS} (Nakanishi, 1979, Sipkin & Revenaugh
 166 1994, Gomer & Okal, 2003). It is also found that apparent attenuation measurements of MODEL 5 and MODEL 1
 167 add up to be exactly equal to MODEL 4, validating the attenuation estimation method in conjunction with the
 168 assumption of $\frac{1}{Q_{apparent}} = \frac{1}{Q_{intr+scat}} = \frac{1}{Q_{intr}} + \frac{1}{Q_{scat}}$.

169

170 Figure 6 compares the levels of scattered coda energy arriving in the vicinity ($\sim \pm 150$ s) of the ScSScS main arrival
 171 generated by different models of mantle heterogeneity models to the synthetic ScSScS predicted by MODEL 1

172 having no scattering. Observing the envelopes of squared velocity for MODEL 2 versus MODEL 4, it is apparent
173 that the levels of energy arriving in the coda and before the main phase significantly increase and the ScSScS pulse
174 width increases due to the presence of increased small-scale heterogeneity in the regions associated with mantle
175 phase changes. It also is important to recognize that intrinsic attenuation can affect the ratio of coda energy to the
176 main pulse. The results for MODEL 5, which omits intrinsic attenuation, demonstrate the importance of intrinsic
177 attenuation for the coda as well as the direct phases. In this case the coda, unaffected by intrinsic attenuation,
178 approaches the amplitude of the direct ScSScS phase.

179

180 **4. Discussion**

181

182 **4.1 Comparison with regional variations**

183 To obtain recordings of clear ScS and ScSScS without interference by depth phases and other arrivals (S, SS, sS),
184 we searched for waveforms of deep focus events in the 10° to 30° distance with moment magnitude > 6 Mw. In
185 supplement Fig. S1 we plot such events available in catalogues of the IRIS DMC from 1970-01-01 to 2019-11-07.
186 The analysis of the waveforms and their codas in the full data set satisfying these conditions would be quite valuable
187 to better constrain predictions regarding the real mantle. The main objective of this study, however, was to a
188 describe a well-defined modeling method and to illustrate how this modeling may be used to constrain the mantle
189 heterogeneity spectrum from ScS and ScSScS waveforms with several observations representative of the range of
190 measured attenuations.

191 Regional variations measured for Q_{ScS} generally fall in the range of 140 – 360 (Nakanishi, 1979, Sipkin &
192 Revenaugh, 1994, Gomer & Okal 2003). Variations on this order are confirmed when we apply our inversion
193 method to two example multiple ScS observations observed from deep focus earthquakes (Fig. 7). We obtain $Q_{ScS} =$
194 153 for an earthquake beneath Papua New Guinea region observed at a station located at Charters Towers in
195 Australia, and $Q_{ScS} = 200$ for an earthquake beneath the eastern China-Russia border region observed at a station
196 located at Yakutsk in eastern Siberia. In Fig. 8 we overlay synthetic seismograms computed from several of our
197 models to determine of how scattering in combination with intrinsic attenuation can affect the relative amplitudes of
198 the direct ScSScS phase and its coda. The heterogeneity power of MODEL 2 inferred from global tomography is too
199 weak to match the excitation of coda relative to ScSScS in both our data examples. Conventional tomographic
200 models typically underestimate true perturbation intensities through the effects of regularization parameters that
201 smooth over the effects of more intense and unresolvable small-scale heterogeneity (e.g., Ritsema et al., 2007).
202 MODEL 4, having PREM attenuation and heterogeneity predicted for a thermodynamic model of the mantle, best
203 matches the relative coda and direct phase excitations for both events. The match can be improved by either a small
204 decrease in intrinsic attenuation or a small increase in heterogeneity power for the eastern China-Russia border
205 region to Yakutsk. ScSn paths from both earthquakes traverse a region of the mantle on the back-arc side of dipping
206 slabs, a southwest dipping slab toward the Australian craton in the case of the New Guinea event (Tregoning and
207 Gorbatov, 2004), and a western dipping Kuril-Kamchatka slab (Koulakov et al., 2011) toward the Siberian craton in

208 the case of the eastern China-Russia border event. The multiple ScSn paths for the eastern China-Russia border
209 event are more slab parallel and distant from the descending slab and more strongly sample the cratonic upper
210 mantle compared to the New Guinea event. Hence, it is likely that the intrinsic attenuation of PREM overestimates
211 the effects of mantle attenuation on ScSn's. Finally, a comparison of observations with the prediction of Model 5,
212 having no intrinsic attenuation, over-predicts coda excitation relative to ScSScS for both events. This confirms that
213 some intrinsic attenuation in the mantle is necessary to dampen the coda generated by the most extreme plausible
214 suggestions of heterogeneity power.

215

216 **4.2 Upper and lower mantle scattering and intrinsic attenuation**

217

218 Strong depth dependence of mantle attenuation, both intrinsic and scattering, has long been documented. Intrinsic
219 attenuation has been found to be relatively low in the mid and deep mantle compared to the upper mantle. Evidence
220 of some scattering in the mid and deep mantle has been confirmed in studies of PKIKP precursors in the 120° to
221 140° great circle range (e.g., Hedlin et al., 1997), including strong regional and depth variations that may be
222 consistent with the effects of either remnant subducted oceanic crust or with a peak in heterogeneity power
223 associated with a post-perovskite phase change. From a study of S and ScS coda, Lee et al. (2003) estimated that
224 scattering attenuation dominates intrinsic attenuation in the lower mantle, reporting their results in terms of the
225 scattering coefficients for a two-layered model of mantle heterogeneity. The scattering coefficients g are related to
226 scattering attenuation by $g = \omega / (Q_{\text{scat}} V_s)$. Our results for MODEL 3 and MODEL 4 show that seismic albedo,
227 the ratio of scattering loss to total attenuation, below 1000 km depth in the mantle is 30 % while above 1000 km it is
228 27 %. This is assuming the PREM average intrinsic shear Q of 225 and 312 for the two depth regions. Hence, we do
229 not observe the scattering to dominate over intrinsic effects in either lower or upper mantle, although regional
230 exceptions can be expected. Additionally, considering the estimated scattering attenuations for MODEL 3 and
231 MODEL 4, we can deduce the scattering coefficients to be $6.25 \times 10^{-5} \text{ km}^{-1}$ for the mantle below 1000 km and 1.256
232 $\times 10^{-4} \text{ km}^{-1}$ for mantle above 1000 km in MODEL 4. These scattering coefficients, calculated for a dominant
233 frequency of 0.05 Hz, are comparable to the low frequency estimates of Lee et al. (2003). This result implies a
234 relatively lower scattering coefficient (i.e. slightly lower scattering attenuation) in the lower mantle compared to the
235 upper mantle in MODEL 4, which agrees with the Lee et al. estimates of scattering coefficients.

236

237 **4.3 Origins of heterogeneity and scale length anisotropy**

238

239 In suggesting that scattering attenuation may dominate intrinsic attenuation throughout the mantle Ricard et al.
240 (2014) considered the effects of heterogeneity distributed primarily in the form of horizontal layers based on
241 geodynamic numerical experiments that predict folding and horizontal stretching of chemical heterogeneity (e.g.,
242 Manga, 1996) whose origin primarily originates from the convective cycling of oceanic crust. The attenuative
243 effects of horizontally layered structure have been well known since the classic paper by O'Doherty and Anstey
244 (1971) and are simply calculated. In this paper, we have instead considered the effects of scale lengths predicted by

245 thermodynamic models in which variations in temperature and chemistry dictate the stability of silicate mineral
246 phases. These variations in temperature and chemistry can also be connected to the convective cycling of oceanic
247 crust, but instead predict that peaks in heterogeneity power will be concentrated near phase transitions. Such models
248 have not yet fully considered the effects of mechanical mixing on the anisotropy of scale lengths within these
249 relatively narrow regions of depth. Nonetheless, thermodynamic models, when verified by observations of scattering
250 effects that supplement tomographic imaging, may at least provide a more reliable estimate of the upper bound to
251 velocity and density fluctuations in the mantle. Experiments similar to ours may be extended to include the effects
252 of anisotropy of scale lengths. Our results indicate that some intrinsic attenuation will always be required to explain
253 the attenuation of body waves, regardless of the state of isotropy of scale lengths.

254

255 **5. Conclusions**

256

257 An inversion algorithm for apparent mantle attenuation based on L2 norm differences between observed and
258 predicted ScSScS velocity waveforms has been verified by inversion of synthetic seismograms and applied to
259 estimate the relative contributions of intrinsic and scattering attenuation to the total apparent attenuation.
260 Thermodynamic models of mantle heterogeneity predict significantly higher heterogeneity power than the
261 predictions from global tomography, and a correspondingly higher relative contribution to apparent attenuation
262 measured from body waves. Taking the depth-dependent heterogeneity power of thermodynamic models of mantle
263 heterogeneity as the maximum plausible heterogeneity we estimate that scattering may explain up to 41.3 % of
264 apparent mantle attenuation with up to 3 % RMS shear velocity perturbations concentrated near mantle phase
265 transitions and 1 % everywhere else. We estimate the scattering contribution to the apparent attenuation from
266 heterogeneity in the upper and lower mantle to be roughly equal in global averages, but regional variations between
267 upper and lower mantle scattering contributions are likely. These estimates agree well with the excitation of coda
268 surrounding ScSn waves observed from deep focus earthquakes. These codas can only be matched by the existence
269 of both intrinsic and scattering attenuation.

270

271 **Data Availability.** The data set of SH component synthetic seismograms can be found at
272 <https://doi.org/10.5281/zenodo.3460694> (Desilva and Cormier, 2019).

273

274 **Acknowledgements.** This work was supported by grants EAR 14-46509 from the National Science Foundation.

275

276 **References**

277

278 Birch F.: Elasticity and constitution of the Earth's interior, *J. Geophys. Res.* 57, 227–286, 1952..

279 Choy, G., and Cormier, V.F.: Direct measurement of the mantle attenuation operator from broadband P and S
280 waves, *J. Geophys. Res.* 91, 7326-7342, 1986.

281 Cormier, V., Li, X., and Choy, G.: Seismic attenuation of the inner core: Viscoelastic or stratigraphic?, *Geophysical*
282 *Research Letters*, 25 (21), 4019-4022, 1998.

283 Cormier, V. F.: D'' as a transition in the heterogeneity spectrum of the lowermost mantle, *Journal of Geophysical*
284 *Research: Solid Earth*, 105(B7), 16193-16205, 2000.

285 Cormier, V.,F., Tian, Y., and Zheng, Y.: Heterogeneity spectrum of Earth's upper mantle obtained from the
286 coherence of teleseismic P waves, *Communications in Computational Physics*, 26(5), 1-27, doi: 10.4208/cicp.OA-
287 2018-079, 2019.

288 Desilva, S. and Cormier. V.: SH component synthetic seismograms (SE_Supplementary_data) (Version v1.0.0)
289 [Data set]. Zenodo. <http://doi.org/10.5281/zenodo.3460695>, 2019.

290 Dziewonski, A. D. and Anderson, D. L.: Preliminary reference earth Model, *Phys. Earth Planet. Inter.*, 25, 297-356,
291 1981.

292 Gomer, B., and Okal, E.: Multiple-Scs probing of the Ontong-Java Plateau, *Physics of the Earth and Planetary*
293 *Interiors*, 138(3-4), 317-331, 2003.

294 Hedlin M A, Shearer P, and Earle P.: Seismic evidence for small-scale heterogeneity throughout the Earth's mantle,
295 *Nature*, 387(6629), 145-150, 1997.

296 Jordan, T. H., and Sipkin S. A.: Estimates of the attenuation operator for multiple ScS Waves, *Geophysical Research*
297 *Letters*, 4(4), 167-170, 1977.

298 Kanamori, H., and Rivera, L.: Nearvertical multiple ScS phases and vertically averaged mantle properties,
299 *interdisciplinary Earth: A Volume in Honor of Don L. Anderson: Geological Society of America Special Paper*, 514
300 and *American Geophysical Union Special Publication*, 71, 9–31, 2015.

301 Kaneshima, S., and Helffrich, G.: Small scale heterogeneity in the mid-lower mantle beneath the circum-Pacific
302 area, *Physics of the Earth and Planetary Interiors*, 183(1-2), 91-103, 2010.

303 Kovach, R. L., and Anderson, D. L.: Attenuation of shear waves in the upper and lower mantle, *Bulletin of the*
304 *Seismological Society of America*, 54(6A), 1855-1864, 1964.

305 Koulakov, I.Y., Dobretsov, N.L., Bushenkova, N.A., and Yakovlev, A.V.: Slab shape in subduction zones beneath
306 the Kurile-Kamchatka and Aleutian arcs based on regional tomography results, *Russ. Geol. and Geophys.*, 52, 650-
307 667, 2011.

308 Lay, T., and Wallace, C.: Multiple scs travel times and attenuation beneath Mexico and Central America, *Geophysical*
309 *Research Letters*, 10(4), 301-304, 1983.

310 Lee, W., Sato, H., and Lee, K.: Estimation of S-wave scattering coefficient in the mantle from envelope
311 characteristics before and after the ScS arrival, *Geophysical Research Letters*, 30(24), 1-5, 2003.

312 Manga, M.: Mixing of heterogeneities in the mantle: Effect of viscosity differences, *Geophysical Research Letters*,
313 23(4), 403-406, doi: 10.1029/96GL00242, 1996.

314 Megnin, C., and Romanowicz, B.: The three-dimensional shear velocity structure of the mantle from the inversion of
315 body, surface and higher-mode waveforms, *Geophysical Journal International*, 143, 709-728, 2000.

316 Nakanishi, I.: Attenuation of multiple ScS waves beneath the Japanese arc, *Physics of the Earth and Planetary
317 Interiors*, 19(4), 337-347, 1979.

318 O'Doherty, R. F. and Anstey, N. A.: Reflections on amplitudes, *Geophys. Prosp.*, 19, 430- 458, 1971.

319 Revenaugh, J., and Jordan, T.: A study of mantle layering beneath the western Pacific, *Journal of Geophysical
320 Research*, 94(B5), 5787-5813, 1989.

321 Ricard, Y., Durand, S., Montagner, J., and Chambat, F.: Is there seismic attenuation in the mantle?, *Earth and
322 Planetary Science Letters*, 388, 257-264, 2014.

323 Ritsema, J., van Heijst, H., and Woodhouse, J.: Global transition zone tomography, *Journal of Geophysical
324 Research: Solid Earth*, 109(B2) , 2004.

325 Ritsema, J., McNamara, A.K., Bull, A.L., Tomographic filtering of geodynamic models: Implications for model
326 interpretation and large-scale mantle structure, *J. Geophys. Res.*, doi: 10.1028/2006JB004566, 2007.

327 Robertson, J.O.A., Blanch, J.O., and Symes, W.W.: Viscoelastic finite-difference modeling, *Geophysics*, 58. 1444-
328 1456, 1994.

329 Sato, H.: Power spectra of random heterogeneities in the solid earth, *Solid Earth*, 10, 275-292, 2019.

330 Shearer, P.: Seismic scattering in the deep Earth, *Treatise on Geophysics Second Edition*, 1, 759-787, 2015.

331 Shearer, P., and Earle, P.: Observing and Modeling Elastic Scattering in the Deep Earth, *Advances in Geophysics*,
332 50(08), 167-193, 2008.

333 Sipkin, S., and Jordan, T.: Regional variation of Qscs, *Bulletin of the Seismological Society of America*, 70 (4),
334 1071-1102, 1980.

335 Sipkin, S., and Revenaugh, J.: Regional variation of attenuation and travel time in China from analysis of multiple-
336 ScS phases, *Journal of Geophysical Research*, 99(B2), 2687-2699, 1994.

337 Stixrude, L., and Lithgow-Bertelloni, C.: Influence of phase transformations on lateral heterogeneities and dynamics
338 in Earth's mantle, *Earth Planet. Sci. Lett.*, 263, 45-55, 2007.

339 Stixrude, L., and Lithgow-Bertelloni, C.: Geophysics of Chemical Heterogeneity in the Mantle, *Annual Review of
340 Earth and Planetary Sciences*, 40(1), 569-595, 2012.

341 Tregoning, P., and Gorbato, A.: Evidence for active subduction at the New Guinea Trench, *Geophys. Res. Lett.*,
342 doi: 10.1029/2004GL020190, 2004.

343 Yoshida, M., and Tsujiura, M.: Spectrum and attenuation of multiply reflected core phases, *Journal of Physics of the
344 Earth*, 23(1), 31-42, 1975.

345 Wu, W., and Irving, J., Using PKiKP coda to study heterogeneity in the top layer of the inner core's western
346 hemisphere, *Geophys. J. Int.*, 209, 672-687, 2017.

347
348 Zheng, Y., and Wu, R.: Theory of transmission fluctuations in random media with a depth-dependent background
349 velocity structure, *Advances in Geophysics*, 50, 21-41, 2008.

350

351

352

353

354

355

356

357

358

359

360

361

362

363

364

365

366

367

368

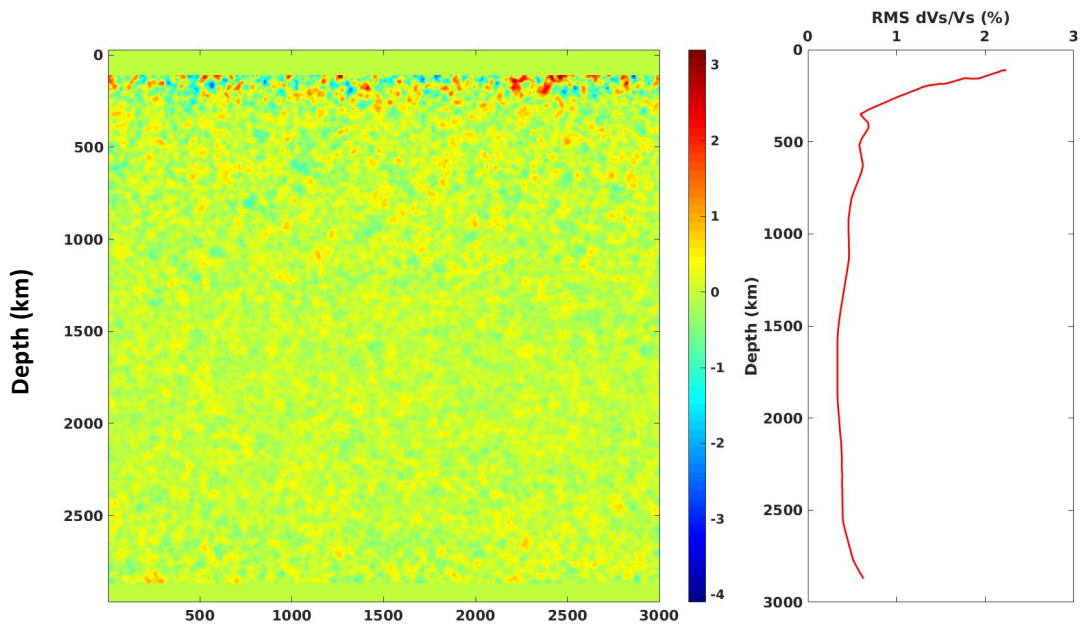
369

370

371

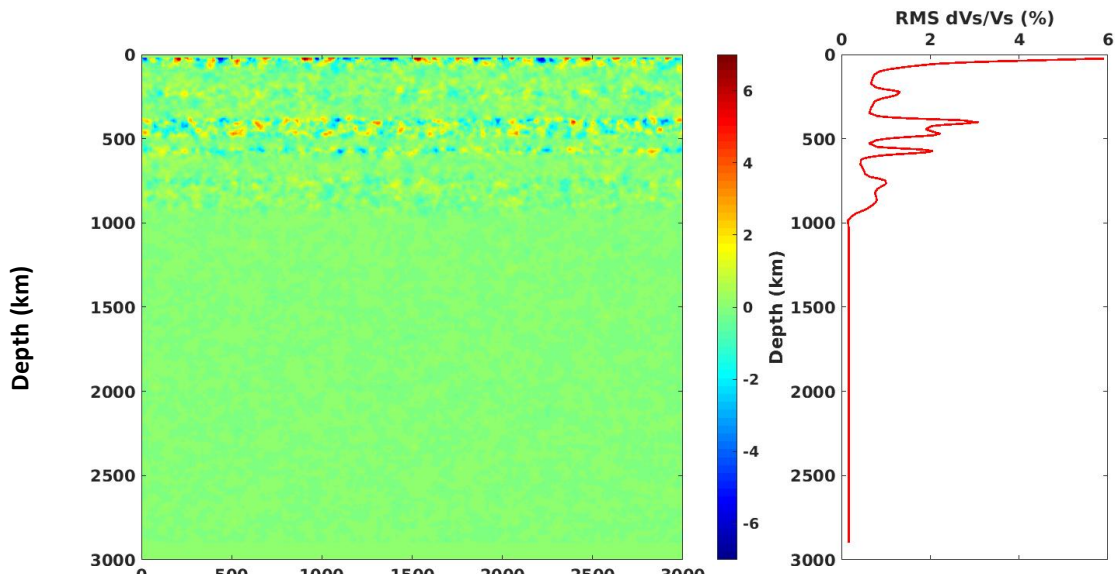
372

373



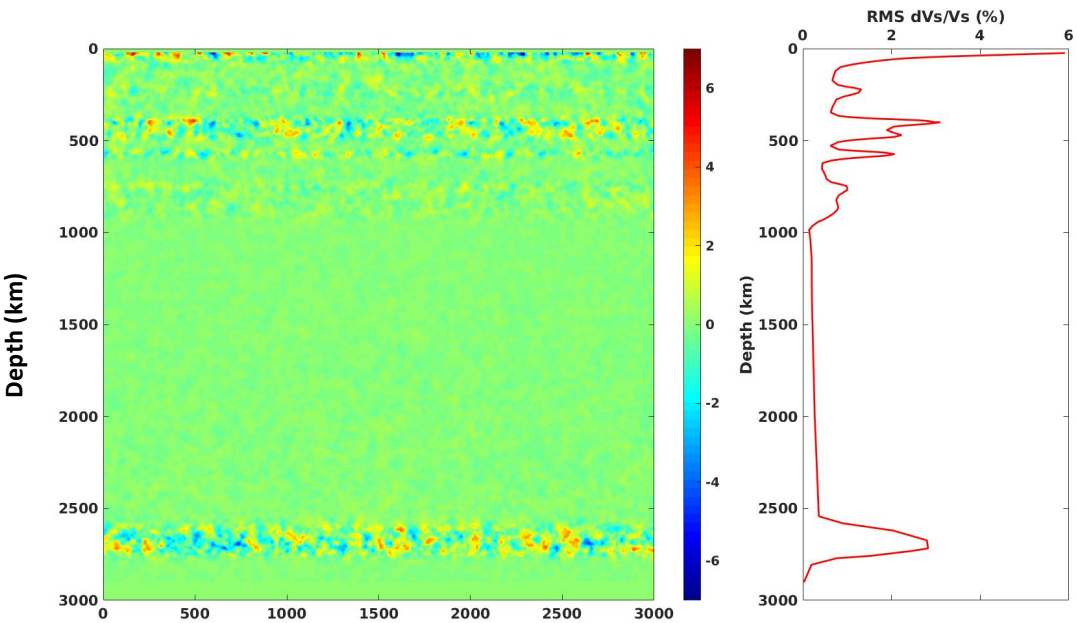
374
375
376
377
378
379
380
381
382
383
384
385
386
387
388
389
390
391
392
393
394
395
396
397
398
399
400
401
402
403
404
405
406
407
408
409
410
411
412
413
414

Figure 1: Right: depth dependent RMS shear velocity perturbation profile applied in Model 2. This is extracted from S20RTS. Left: 2D representation of the same depth dependent profile. Heterogeneous media is for an exponential autocorrelation (corner scale $a = 10$ km) function. Note the increase in heterogeneity power near the top and bottom of the mantle.



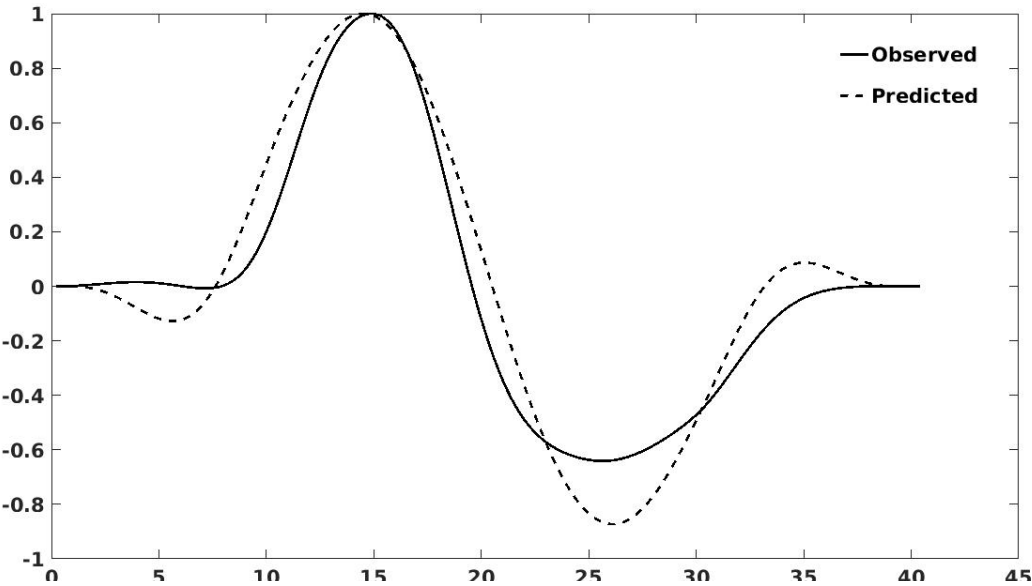
415
416
417
418
419
420
421
422
423
424
425
426
427
428
429
430
431
432
433
434
435
436
437
438
439
440
441
442
443
444
445
446
447
448
449
450
451
452
453
454
455

Figure 2: Right: Depth dependent RMS shear velocity perturbation profile applied in Model 3 vs. perturbation values from crust to 1000 km depth is extracted from the stochastic tomography result of Cormier et al. (2019). Left: 2D representation of the same depth dependent profile. Compared to Model 2 note the additional peaks in heterogeneity power associated with phase transitions in the upper mantle.



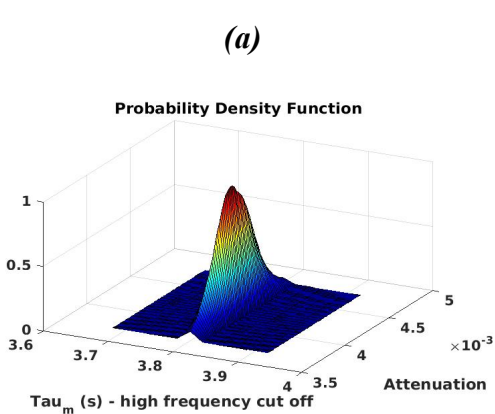
456
457
458
459
460
461
462
463
464
465
466
467
468
469
470
471
472
473
474
475
476
477
478
479
480
481
482
483
484
485
486
487
488
489
490
491
492
493
494
495
496

Figure 3: Right: Depth dependent RMS shear velocity perturbation profile applied in Model 4 vs. perturbation values from crust to 1000 km depth is extracted from the stochastic tomography result of Cormier et al. (2019). Compared to Model 3 an additional peak is added near the core mantle boundary to incorporate the increased lower mantle associated with the post-perovskite phase change (Stixrude & Lithgow-Bertelloni, 2012) Left: 2D representation of the same depth dependent profile.

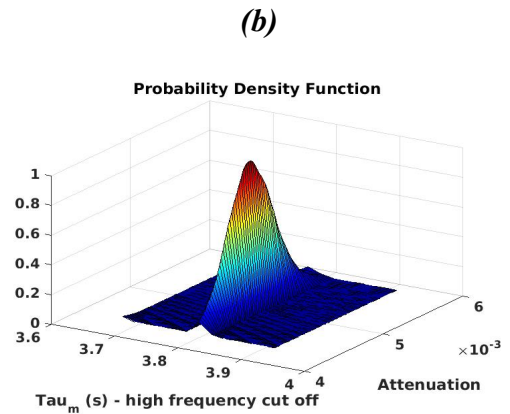


497
498
499
500
501
502
503
504
505
506
507
508
509
510
511
512
513
514
515
516
517
518
519
520
521
522
523
524
525
526
527
528
529
530
531
532
533
534
535
536
537
538

Figure 4: Observed and predicted ScSScS velocity waveform aligned by the arrival time of first extremum and normalized by the peak to trough amplitude. The least squares norm difference between these two waveforms is obtained using a summation of amplitude differences over time.

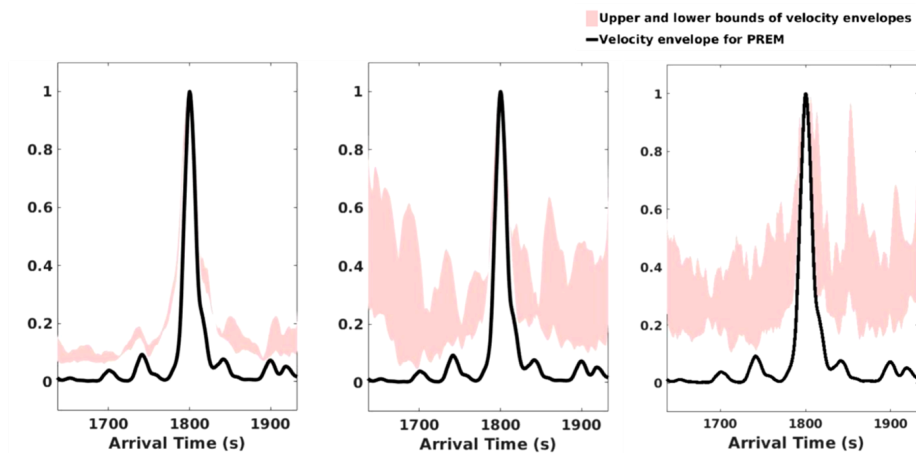


15



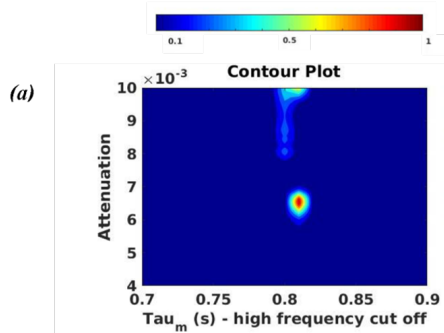
539
540
541
542
543
544
545
546
547
548
549
550
551
552
553
554
555
556
557
558
559
560
561
562
563
564
565
566
567
568
569
570
571
572
573
574
575
576
577
578
579

Figure 5: Gaussian probability density function constructed with the least squares norm difference between predictions and simulated observations for (a) MODEL 1, (b) MODEL 2, (c) MODEL 3, (d) MODEL 4 and (e) MODEL 5.



580
581
582
583
584
585
586
587
588
589
590
591
592
593
594
595
596
597
598
599
600
601
602
603
604
605
606
607
608
609
610
611
612
613
614
615
616
617
618
619
620
621

Figure 6: Upper-lower bounds of coda envelopes (shaded area) calculated from 5 random heterogeneity realizations of each MODEL 2 (left), MODEL 4 (middle) and MODEL 5 (right), compared to PREM (black line).



622
623
624
625
626
627
628
629
630
631
632
633
634
635
636
637
638
639
640
641
642
643
644
645
646
647
648
649
650
651
652
653
654
655
656

Figure 7: Contour plots of probability density functions obtained with multiple ScS observations in two regions. Event (circles) and IU station (triangles) locations for the two regions described below are shown in panel (c).

- (a) Mantle beneath Papua New Guinea region : Observations are recorded by station CTAO (146.25° E, 20.08° S) for a 490 km deep, mw 6.6 event (154.88° E, 45.43° S) which occurred on May 02 1998, 13:34:28 UTC. Event-station distance is 17.6° .
- (b) Mantle beneath Eastern China-Russia border region : Observations are recorded by station YAK (129.68° E, 62.03° N) for a 568 km deep, mw 7.3 event (130.66° E, 43.76° N) which occurred on June 28 2002, 17:19:30 UTC. Event-station distance is 18.3° .

657
658
659
660
661
662
663
664
665
666
667
668
669
670
671
672
673
674
675
676
677
678
679
680
681
682
683
684
685
686
687
688
689
690
691
692
693
694
695
696
697
698

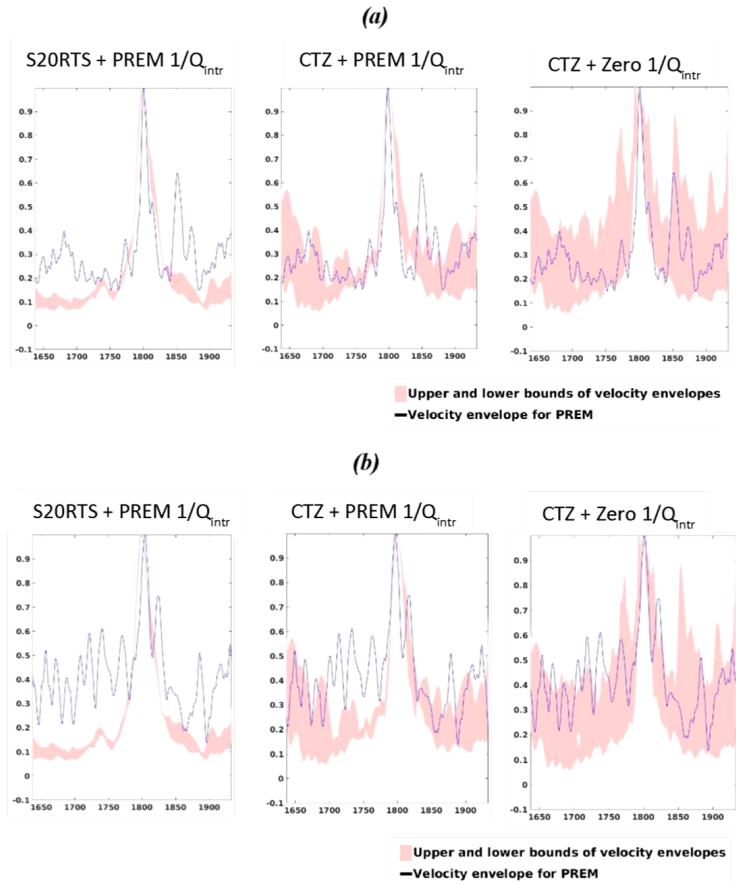


Figure 8: Upper-lower bounds of coda envelopes (shaded area) calculated from 5 random heterogeneity realizations of each MODEL 2 (left), MODEL 4 (middle) and MODEL 5 (right), compared to the squared velocity envelopes of data traces (solid blue lines) from (a) Papua New Guinea data and (b) Eastern China-Russia border region.

699
700
701
702
703
704
705
706
707
708
709
710
711
712
713
714
715
716
717
718
719
720
721
722
723
724
725
726
727
728
729
730
731
732
733
734
735
736
737
738
739

	$Q_{SeS} \pm \delta Q_{SeS}$	$\tau_m \pm \delta \tau_m$ (sec)
MODEL 1	0.004167 ± 0.00028	3.800 ± 0.004
MODEL 2	0.005000 ± 0.00034	3.790 ± 0.004
MODEL 3	0.005747 ± 0.00066	4.600 ± 0.010
MODEL 4	0.007100 ± 0.0005	3.630 ± 0.007
MODEL 5	0.002900 ± 0.0003	1.980 ± 0.005

Table 1 : Apparent attenuation parameters and their errors estimated for the five simulated models using probability density functions shown on Fig. 5..

	Q_{Scs}	<u>Scattering Attenuation</u> <u>Apparent Attenuation</u>	<u>Intrinsic Attenuation</u> <u>Apparent Attenuation</u>
MODEL 1 (PREM)	240		100 %
MODEL 2 (Tomographic dVs/Vs model (exponential ACF, a = 10km) + PREM)	200	16.7 %	83.3 %
MODEL 3 (Thermodynamic dVs/Vs model for UM only (exponential ACF, a= 10 km) + PREM)	174	27.5%	72.5%
MODEL4 (Thermodynamic dVs/Vs model for both UM and LM (exponential ACF, a = 10 km) + PREM)	140	41.3 %	58.7 %
MODEL 5 (Thermodynamic heterogeneity + no intrinsic attenuation + PREM velocities and densities)	340	100 %	

740
741
742
743
744
745
746

Table 2 : Estimated relative contributions to apparent $1/Q_{Scs}$.